Research Square

Preprints are preliminary reports that have not undergone peer review.
They should not be considered conclusive, used to inform clinical practice,
or referenced by the media as validated information.

Synthesis of ZIF-8@g-C 3 N 4 nanomaterial and its use for rapid removal of alizarin red and ketoprofen from water via chemical catalysis

ayşe bayrak
Selçuk University
sevde demir
Eskişehir Osmangazi University
hakan erer
Eskişehir Osmangazi University
ilkay hilal gübbük
ihilalg@gmail.com

Selçuk University
mustafa ersöz
Selçuk University

Research Article

Keywords: ZIF-8, g-C3N4, nanoparticle, degradation, drug, dye

Posted Date: April 15th, 2026

DOI: https://doi.org/10.21203/rs.3.rs-9093452/v1

License: This work is licensed under a Creative Commons Attribution 4.0 International License.
Read Full License

Additional Declarations: No competing interests reported.

Version of Record: A version of this preprint was published at Research on Chemical Intermediates on August 18th, 2026. See the published version at https://doi.org/10.1007/s11164-026-06082-0.

Synthesis of ZIF-8@g-C_3N_4 nanomaterial and its use for rapid removal of alizarin red and ketoprofen from water via chemical catalysis

Ayşe Bayrak[1], Sevde Demir[2], Hakan Erer[2], Ilkay Hilal Gubbuk[1*], Mustafa Ersoz[1]

[1]Faculty of Science, Department of Chemistry, Selcuk University, Campus, 42075, Konya, Türkiye

[2]Faculty of Science, Department of Chemistry, Eskisehir Osmangazi University, Eskisehir, Türkiye

Corresponding Author: ilkayg@selcuk.edu.tr, ihilalg@gmail.com

+90 (332) 2233859

ORCID ID: 0000-0001-7061-2588

Ayşe Bayrak: bayrakayse123@gmail.com

Sevde Demir: sevdecamur@gmail.com

Hakan Erer: hakanerer81@gmail.com

Mustafa Ersoz: ersozm@gmail.com

Abstract

The development of a new catalyst for highly efficient degradation of environmentally harmful pollutants is targeted. In this study, g-C_3N_4@ZIF-8 catalyst was produced to reduce both the widely used drug ketoprofen (KEP) and the harmful organic dye impurity alizarin red (ARS) from aqueous solutions. In this system using g-C_3N_4@ZIF-8 as the catalyst, the degradation of both KEP and ARS by a rapid chemical and heterogeneous catalytic reaction was attributed to the synergistic interaction of the two components in the g-C_3N_4@ZIF-8 catalyst.

In this study, graphitic carbon nitride doped nanoparticles containing ZIF-8 from the MOF group containing Zn metal were synthesized by easy calcination and their characterization was completed both structurally and superficially. The synthesized g-C_3N_4@ZIF-8 nanoparticle was used as a catalyst for the catalytic degradation of ARS and KEP with $NaBH_4$. The synthesized g-C_3N_4@ZIF-8 was analyzed by X-ray diffraction (XRD), infrared spectrometry (ATR-FTIR), XPS solid phase UV-DRS spectroscopy, Atomic force microscopy (SEM-EDX Fourier Transform Infrared and zero charge point pH). Optimum parameters were determined by investigating the effects of catalyst amount, $NaBH_4$ concentration, contact time and pH on the removal mechanism. The kinetics of ARS and KEP removal in the g-C_3N_4@ZIF-8 nanocatalyst were calculated using a pseudo-first-order model and appropriate experimental data. A pseudo-first-order kinetic model was used to describe dye and drug removal, and graphs showing the change between $ln[C_0/C_t]$ and time were drawn.

Key words: ZIF-8, g-C_3N_4, nanoparticle, degradation, drug, dye.

1. Introduction

In recent years, with the intensification of urbanization and rapid development of industrialization, the ecological environment has been seriously damaged. Organic pollutants, especially those found in environmental wastewater, such as pharmaceuticals, household waste, and dye waste from both food and textiles, are carcinogenic and mutagenic and pose a great threat to water resources. Water pollution and water scarcity are one of the most important and urgent environmental problems facing humanity today (Li et al., 2022; Yuan et al.2021). These wastewaters can cause serious harmful effects for the environment due to the high toxicity and chemical resistance they contain (Payra et al., 2021). Water pollution occurs when natural and human-induced factors come together and harms ecosystems, human health and the economy. Dye wastewater is generated during the production and

application of dyes, and an effective dye degradation technology and suitable catalyst materials must be found to remove it from water (Ma et al., 2021).

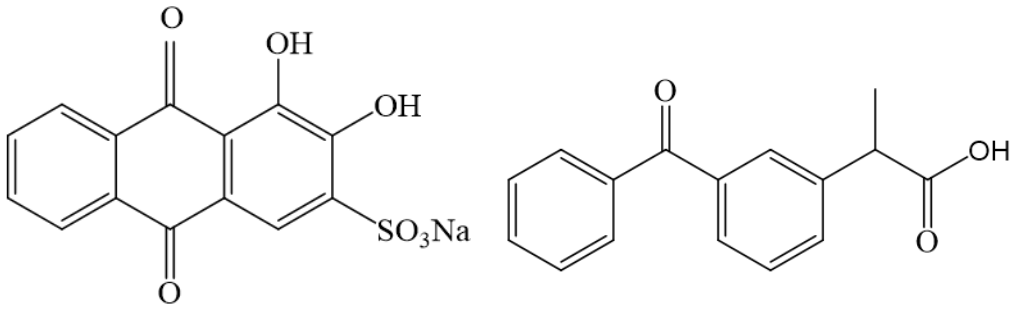
Alizarin red-S (ARS) is dyestuffs generally used in large quantities for dyeing textiles, leather, paper and other materials. ARS is an anionic dyes that cause many environmental problems resulting in environmental pollution in wastewater. Among these organic dyes containing the anthraquinone ring as the basic structure, ARS (1,2-dihydroxy-9,10-anthraquinonesulfonic acid sodium salt) is one of the widely used dyes, originally obtained from the root of the madder plant. It is resistant to degradation due to its complex and aromatic structure and high thermal and chemical stability. It is soluble in water and alcohol, some forms are carcinogenic, and it is resistant to degradation due to its complex aromatic structure and high thermal and optical stability (Rani et al., 2017). The cyclic structure of alizarin red is mainly based on the 1,2-dihydroxyanthraquine ring of alizarin, but this structure is modified by functional groups added to alizarin. This derivatization process helps change the color and solubility properties of alizarin red. Most treatment methods developed against this type of dye, whose complex structure of aromatic rings makes it resistant to degradation, have been largely inadequate. If inhaled or ingested, ARS can cause irritation of mucous membranes, especially in the lungs, eyes, skin, and respiratory tract, and cause other serious health problems (Gholivand et al., 2015; Gautam et al. 2013).

Pharmaceuticals are an essential group of contaminants due to their widespread use and presence in drinking water and freshwater sources, and their toxic effects on ecosystems and humans. Extensive studies conducted in the last years have shown that purified drinking water contains a variety of pharmaceutical contaminants such as antiepileptics, hormones, vitamins, analgesic and anti-inflammatory drugs, and antibiotics (Ahmed et al., 2021).

Nonsteroidal antiinflammatory drugs are a group of medications that are effective in reducing inflammation, pain, and fever in the body. Because wastewater treatment plants (WWTPs) cannot effectively remove pharmaceutical contaminants such as ketoprofen, these compounds are frequently detected in the aquatic environment. Ketoprofen (2-(3-benzoylphenyl)-propanoic acid) (Figure 1) is one of the most widely used anti-inflammatory drugs widely used to treat pain, fever, and inflammation and is frequently detected in wastewater and surface water (Mei et al., 2025).

KEP is a nonsteroidal antiinflammatory drug widely used in the treatment of headaches, rheumatoid arthritis, osteoarthritis, ankylosing spondylitis (Atzeni et al., 2021). In the chemical structure of Ketoprofen, there is a region called the chromophore, with a light-sensitive chromophore called benzophenone. The benzophenone region in

the chemical structure of ketoprofen sensitizes the drug to UV light, causing undesirable photoallergic effects such as hypersensitivity and myasthenia gravis on human skin (Martinez et al., 2013).



(a) *(b)*

Fig. 1. Molecular structure of Alizarin Red (a) and ketoprofen (b) 2D structure

MOFs have promising potential in different fields such as gas storage, sensor, adsorption, antibacterial, drug delivery, water purification, energy storage and catalysis (Bag et al., 2020). MOFs are suitable candidates for many different applications as catalysts due to their high porosity, surface area, and chemical structure. The wide structural diversity of MOFs is achieved by using different metal ions, organic ligands and configuration strategies (Verma et al., 2023; Chirra et al., 2021). MOFs have chemically tunable properties for catalytic applications due to their structure consisting of various metal clusters and organic linkers. These properties make MOFs suitable for different catalytic applications.

ZIFs are a class of materials with numerous applications because they exhibit properties such as high and homogeneous pore size distribution, crystalline structure, micropores, and high thermal and chemical stability. ZIFs are often preferred because they offer greater adaptability for the design of hybrid metal-organic framework structures due to their high surface area and functionality. ZIFs are microporous materials with broad application areas that combine the unique properties of both zeolites and MOFs (Chirra et al., 2021). ZIFs are MOF structures that are typically formed by reacting zinc (Zn) or cobalt (Co) as metal sources with imidazole or imidazole derivatives as organic ligands in a solvent (Chen et al., 2014).

The 3D network structure of ZIF-8, tetrahedrally coordinated with zinc-centered methylimidazole linkers, provides the catalytically active site and vertical surface area. Additionally, the framework structure of ZIF-8 may serve as

a template for further modification and functionalization. ZIF-8 is hydrophobic and has high chemical and hydrothermal stability and it can still maintain structural stability when the temperature is up to 500 °C, and can also maintain its crystallinity and porosity after being placed in various solutions such as water and organic solvents (Banerjee et al., 2009; Schelling et al., 2020). The ZIF-8 compound has high porosity, high surface area and easily adaptable pore structures, allowing it to be optimized for the desired application with easily adaptable pore sizes. ZIF-8 materials have been widely used in many forms, including particles, colloids, membranes or thin films, and have been applied to various important fields such as catalysis, drug delivery, sensor, etc. (Schelling et al., 2020). Although ZIF-8 has important properties on its own, combining this material with different supports in a controllable manner enables the creation of composite or hybrid materials with new and advanced properties, and these materials attract wide attention (Lu et al., 2012; Li et al., 2018).

Among many supporting materials, graphitic carbon nitride (g-C_3N_4), a metal-free polymer semiconductor composed of carbon and nitrogen elements, is easy and low-cost to synthesize. The g-C_3N_4 composite formed with ZIF-8 (g-C_3N_4@ZIF-8) is widely applied in dye removal due to its thermal and chemical stability, large surface area and high porosity (Zheng et al., 2021). Graphite carbon nitride (g-C_3N_4) nanosheets have great potential in water splitting, carbon dioxide reduction, degradation of organic pollutants and catalytic studies due to their absorbance and charge separation in dispersed suspension and band gap (2.7 eV) suitable for applications. Nitrogen-based compounds such as melamine, thiourea, or urea are often used as precursors in the synthesis of g-C_3N_4. Their economical, practical one-pot preparation method and high chemical and thermal stability enable g-C_3N_4 to be successfully applied in the fields of catalytic degradation of pollutants, electrocatalysis, and energy storage and conversion (Zhou et al., 2019).

There are some studies in the literature involving ZIF-8 and g-C_3N_4. In these studies, g-C_3N_4 was used as a support surface and ZIF-8 was used to increase catalytic performance. A review of most studies in the literature revealed that no study has used the g-C_3N_4@ZIF-8 composite for chemically catalytic degradation in the presence of $NaBH_4$ and without light. Some studies have incorporated different metals into the composite to enhance photocatalytic performance. One study used the composite alone, while the present study investigated the photocatalytic degradation of tetracycline. Therefore, the present study is not yet available in the literature, both in terms of chemical catalysis and the types of pollutants reduced (Mahmoodi et al., 2025; Asadi et al., 2022; Yaseen et al., 2025).

The main objectives of this study are the preparation and detailed characterization of ZIF-8 and g-C_3N_4 modified ZIF-8 heterostructures, and their subsequent catalytic use. In the presented study, the characterization of ZIF-8 and pure g-C_3N_4, as well as the g-C_3N_4@ZIF-8 composite, is carried out using techniques such as XRD, FTIR, SEM-EDX, UV-DRS, and XPS analysis. Finally, the use of the g-C_3N_4@ZIF-8 catalyst for the chemical degradation of alizarin red and ketoprofen is carried out. The composite used in this study, g-C_3N_4@ZIF-8, has not been previously used in the literature for the removal of ARS and KEP via chemical catalysis. This is the first study to demonstrate the catalytical use of g-C_3N_4@ZIF-8 in the presence of $NaBH_4$ by chemical catalysis.

2. Materials and methods

2.1. Materials

Melamine, zinc nitrate hexahydrate, 2-methylimidazole, ethanol, alizarin red, ketoprofen, NaOH, HCl, and NaCl were purchased from Sigma Aldrich. Deionized water and chemicals purchased without further purification were used during the experiments.

The structural features and composition of the ZIF-8, g-C_3N_4 and g-C_3N_4@ZIF-8 were identified with a X-ray diffractometer (Bruker D8 ADVANCE XRD; source: Cu Kα1 radiation with λ = 1.5406 Å; scan rate: = 2 min−1, 40 kV, 40 mA) using Cu K radiation. FTIR spectra of the three samples were characterized using a Perkin Elmer model 100 ATR-FTIR spectrophotometer. Morphological features were observed using SEM device (5600-LU SEM, JEOL, UK). For catalytic performance studies, UV–vis diffuse reflectance spectra of the samples were recorded on a UV-1700 spectrometer (Shimadzu, Japan). To determine the electronic properties of the catalyst, UV-visible diffuse reflectance spectra (UV-vis DRS) were measured using a Shimadzu UV-3600 Plus UV-Vis-NIR Spectrophotometer. The chemical states of the elements in the g-C_3N_4@ZIF-8 composite and the valence band of the samples were examined by Thermo Fisher X-ray photoelectron spectroscopy (XPS) to reveal the interactions between g-C_3N_4 and ZIF-8. After catalysis with the g-C_3N_4@ZIF-8 composite, the concentration of the remaining ARS and KEP solution was determined by high-performance liquid chromatography (HPLC LC-20AD, Shimadzu, Japan).

2.2. Synthesis of the ZIF-8

ZIFs were synthesized by the solvothermal synthesis method according to the literature (Park et al., 2006). **Z**inc nitrate tetrahydrate ($Zn(NO_3)_2 \cdot 4H_2O$) (0.210 g, 8.03 x 10^{-4} mol), 2-methylimidazole (H-MeIM) (0.060 g, 7.31 x 10^{-4} mol) and 18 mL of DMF were taken into a 50 mL beaker and stirred at 50 °C for 30 minutes. Then, the reaction

mixture was transferred to Teflon-coated sealed acid digestion bombs and placed in an oven set at 140 °C with a temperature increase of 5 °C/min. After 24 hours the mixture was cooled and filtered. The resulting solid was washed with DMF (10 mL x 3) and dried.

2.3. Synthesis of g-C_3N_4

Melamine (more than 99% purity) was purchased from Sigma-Aldrich. g-C_3N_4 was successfully synthesized in a furnace by a simple heating method according to literature (Figure 2) (Zhou et al., 2014; Xue et al., 2019). In the synthesis of g-C_3N_4, 5 g of melamine powder was obtained by heating in a covered alumina crucible at 550 ˚C for 4 h with a heating rate of 10 ˚C/min (Wang et al., 2019). When the crucible was cooled to room temperature, g-C_3N_4 powder was obtained as a pale yellow powder (Ma et al., 2015). The heating temperature used in the experiments varied between 500 °C and 550 °C, and the heating rate was 10 °C/min. As the temperature increased, the characteristic color of the crystallization of the deterioration darkened and a more perfect crystallization was achieved (Zhao et al., 2018).

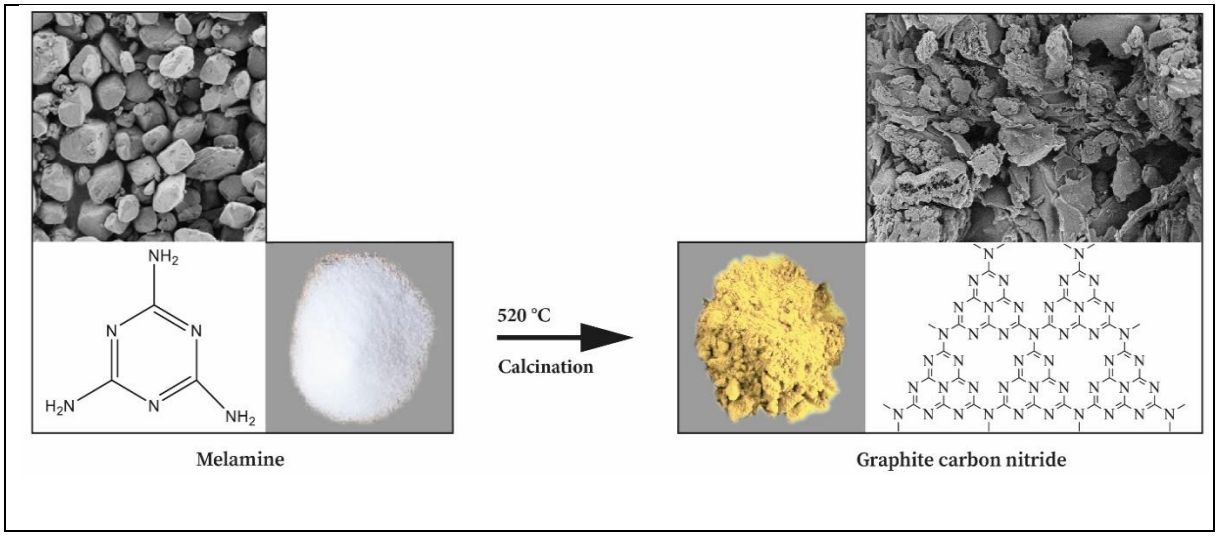


Fig. 2. Schematic representation of g-C_3N_4 synthesis from melamine.

2.4. Synthesis of g-C_3N_4@ZIF-8

g-C_3N_4@ZIF-8 composite was prepared according to the method described in the literature. ZIF-8 and g-C_3N_4 with different morphologies were combined to produce binary heterostructure composites that utilize the properties of both materials (Sharma et al., 2023). For the synthesis of g-C_3N_4@ZIF-8, firstly, light yellow g-C_3N_4 precipitate

was obtained from melamine calcination. ZIF-8 was added to the mixture of melamine and ethanol and stirred on a magnetic stirrer until a homogeneous distribution was achieved. It was then heated to 70°C to evaporate the ethanol (Guo et al., 2019). The resulting homogeneous mixture was placed in a 15 mL crucible for calcination and gradually heated at a 50°C heating rate in 5 min. Once the temperature reached 520°C, it was held at this temperature for 3.30 h (Xu et al., 2023; He et al., 2024). The obtained product (g-C_3N_4@ZIF-8) was powdered and stored in a closed environment. Figure 3.

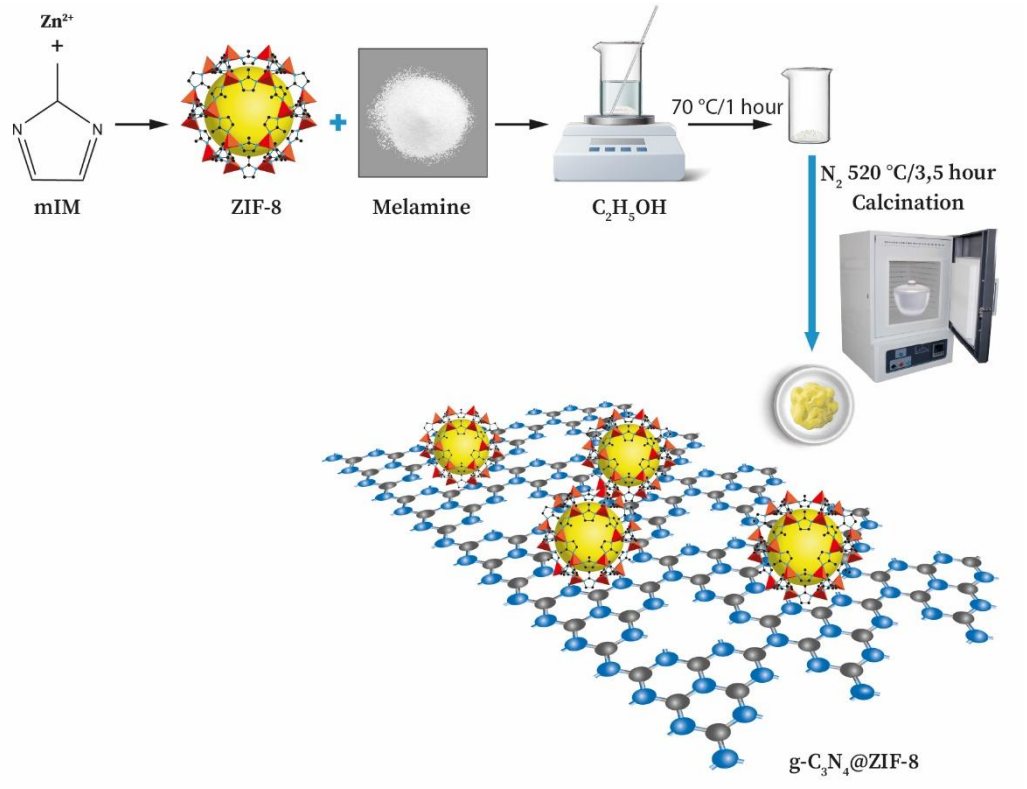


Fig. 3. Schematic representation of g-C_3N_4@ZIF-8 nanoparticle synthesis

2.5. Catalytic experiment

The catalytic reduction property of g-C_3N_4 and g-C_3N_4@ZIF-8 were evaluated by the following procedure. Both ARS and KEP, mixtures of $NaBH_4$ solution and particles selected as contaminants, were monitored over time on a UV-Vis spectrometer for catalysis experiments and the spectra were recorded. In the experimental setting, 1 mg of catalyst, 1.0 10^{-1} M $NaBH_4$ and 0.9 mL of deionized water were added to a solution containing 1 mL of 1.0×10^{-4} M ARS or KEP. The degradation of the pollutant was monitored by the decrease of the absorbance maximum at 524 nm for ARS and at 260 nm for KEP. The catalytic reduction reaction was monitored over a 1 min time period

using a UV-visible spectrophotometer. Degradation studies were also conducted without the use of NaBH4 and nanoparticles. The conversion efficiency of ARS and KEP reduction was calculated by equation (Eq. 1) (Lin et al., 2024).

$$Degradation(\%) = \frac{(A_0 - A_t)}{A_0} \quad (1)$$

where, A_0 and A_t are the absorbance of ARS and KEP at the initial and periodic time intervals, respectively. Kinetic calculations of degradation were also performed for both ARS and KEP. The (k) rate constant (min^{-1}) of the catalytic reduction was determined by employing equation (Eq. 2) (Suresh et al., 2023).

$$\ln\left(\frac{A_t}{A_0}\right) = -kt \quad (2)$$

where, t is a particular time (min). A plot of $\ln(A_t/A_0)$ versus t was drawn and fitted with a simulated linear line to find the rate constant value.

3. Conclusion

3.1. Characterization

g-C_3N_4, ZIF-8, and their composite g-C_3N_4@ZIF-8 were synthesized and characterized using different techniques in this study. g-C_3N_4 was synthesized starting from melamine precursors, and then its composite was synthesized with ZIF-8. Detailed characterization of both the precursor and the composite is presented below.

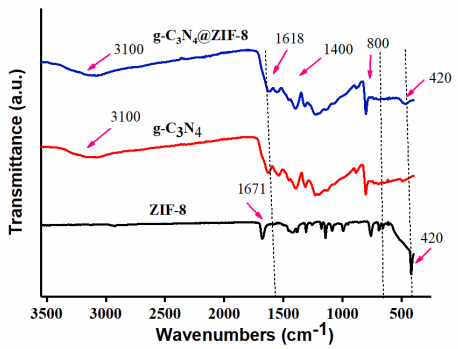


Fig. 4 (a) Comparative FTIR spectra of pure ZIF-8 and pure g-C_3N_4 and ZIF-8@g-C_3N_4

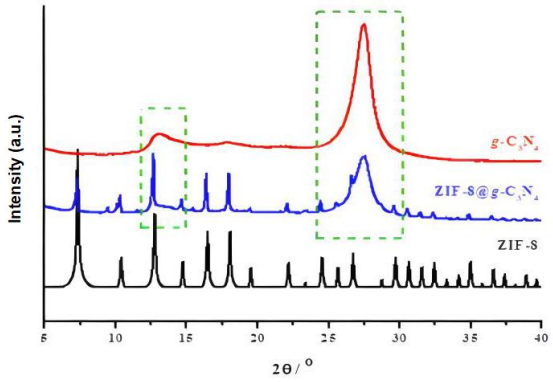


Fig. 4 (b) Comparative XRD Analysis of Pure ZIF-8 and Pure g-C_3N_4 and ZIF-8@C_3N_4

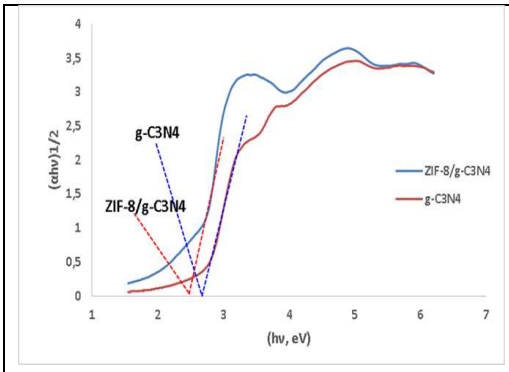


Fig. 4 (c) Absorbance spectra of g-C_3N_4 and g-C_3N_4@ZIF-8

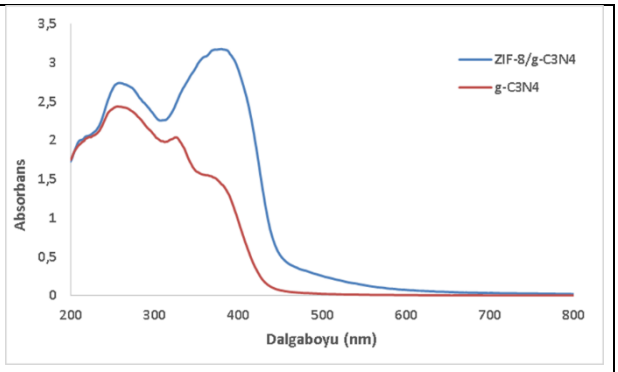


Fig. 4 (d) Tauc plots and band gaps of g-C_3N_4 and g-C_3N_4@ZIF-8 molecules.

FTIR spectra of ZIF-8, g-C_3N_4 and g-C_3N_4@ZIF-8 molecules are shown in Figure 4(a). In the FTIR spectrum of g-C_3N_4, which has a polymeric structure, the characteristic vibration of the triazine ring at approximately 810 cm^{-1}, the broad peak group in the range of 1200-1650 cm^{-1} represents the stretching vibrations of the C-N and C=N bonds in the aromatic structure, and the N-H stretching vibrations of the amino groups on the g-C_3N_4 surface in the range of 3000-3300 cm^{-1} (Jomekian et al., 2020). In the FTIR spectrum of ZIF-8, the peaks are those of the Zn-N bonds at 421 cm^{-1}, and those of the C-N and C=N groups in the 1000-1600 cm^{-1} range. In the FTIR spectrum of the composite structure g-C_3N_4@ZIF-8, characteristic peaks are observed for both g-C_3N_4 and ZIF-8 (Li et al., 2024). This suggests that interactions related to the synthesis of the composite have occurred. The peak observed at 1400 cm^{-1} in the composite indicates ring stretching, while the peaks in the 750-690 cm^{-1} range correspond to in-plane ring bending modes. The peaks appearing at 750 and 800 cm^{-1} were attributed to the aromatic C-H bending. The strong peak at 420 cm^{-1} can be attributed to the C-N bending vibration and the Zn-N stretching vibration of imidazole, respectively (Qiu et al., 2021). The broad peak observed in the 3500-3200 cm^{-1} range indicates stretching vibration of the N-H bonds. However, due to the low ZIF-8 content in the composite material, a decrease in the intensity of the characteristic peaks of ZIF-8 was observed. In addition, the peaks between 1200 cm^{-1} and 1650 cm^{-1} corresponded to the stretching of CN heterocycles, and the peaks at 1650 cm^{-1} (C=C) and 3350 cm^{-1} (O-H) were associated with g-C_3N_4. All these findings proved that g-C_3N_4@ZIF-8 nanocomposite was synthesized successfully (Karimi-Maleh et al., 2022).

The characteristic XRD peaks of ZIF-8, g-C_3N_4 and g-C_3N_4@ZIF-8 are seen in Figure 4(b). In the XRD spectrum of ZIF-8, peaks are seen at 7.281, 10.31, 12.66, 14.71, 16.41, 17.961, 22.11, 24.51 and 26.71 degrees. As can be seen from the XRD spectra of g-C_3N_4, the extensive diffraction peaks occurring at 2θ values of 13.1° and 27.4° were attributed to the (100) and (002) planes, respectively. The peaks in g-C_3N_4@ZIF-8 composite, but not in g-

231 C_3N_4, are seen as 10.31, 14.71, 16.41, 17.961, 22.11. The strong diffraction peaks in g-C_3N_4@ZIF-8 molecules
232 indicate their excellent crystallinity, ZIF-8 was deposited on g-C_3N_4, and the small shift in the XRD pattern of g-
233 C_3N_4composite can be attributed to the incorporation of ZIF-8 into the g-C_3N_4 structure and/or the interactions
234 between g-C_3N_4 and ZIF-8 at the interface. The presence of these peaks observed in ZIF-8 and g-C_3N_4 in the
235 composite also confirms that g-C_3N_4@ZIF-8 was successfully synthesized (Yuan et al., 2021; Liu et al., 2018; Qiu
236 et al., 2021; Abed and Amar; Li et al., 2022). Additionally, the crystal size of g-C_3N_4@ZIF-8 was recorded as 6.72
237 nm using the Debye-Scherrer equation (3).

238
$$D_{111} = \frac{k\lambda}{(\beta cos\theta)} \quad (3)$$

239 where, *D* is crystallite size, *k* (0.891*)* is Debye-Scherrer's constant, *λ* ((1.5406 Å for CuKα radiation) stands for X-
240 ray wavelength, β indicates the full width at half maximum intensity (*FWHM*) of the XRD peaks and θ is the
241 11iffraction angle (*2θ)*.
242 Figure 4(c-d) shows the UV-visible DRS spectra of g-C_3N_4 and g-C_3N_4@ZIF-8 compounds. The absorption
243 spectra of Bgcn show a moderate absorption range throughout the entire visible spectrum. g-C_3N_4 compound shows
244 less visible light absorption than g-C_3N_4@ZIF-8 and the absorption edge is shifted towards 450 nm in the visible
245 spectrum. The change in optical properties of g-C_3N_4@ZIF-8 molecule due to ZIF-8 doping is considered as
246 evidence of binding of two molecules. Figure 4(d) shows the tauc plot and the band gap energy of g-$C_3N_4$and g-
247 C_3N_4@ZIF-8 molecules is calculated by using Kubelka-Munk method. The band gaps of g-C_3N_4 and g-C_3N_4@ZIF-
248 8 are 2.6 and 2.7 nm, respectively. The energy gap of g-C_3N_4@ZIF-8 is found to be smaller than that of g-C_3N_4
249 (Sairaj et al., 2024).
250

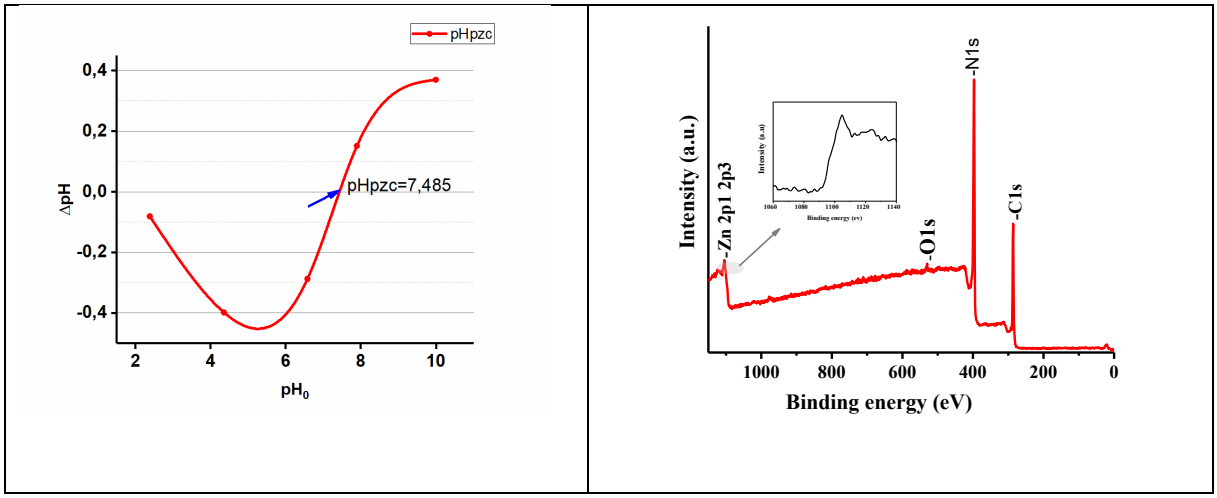
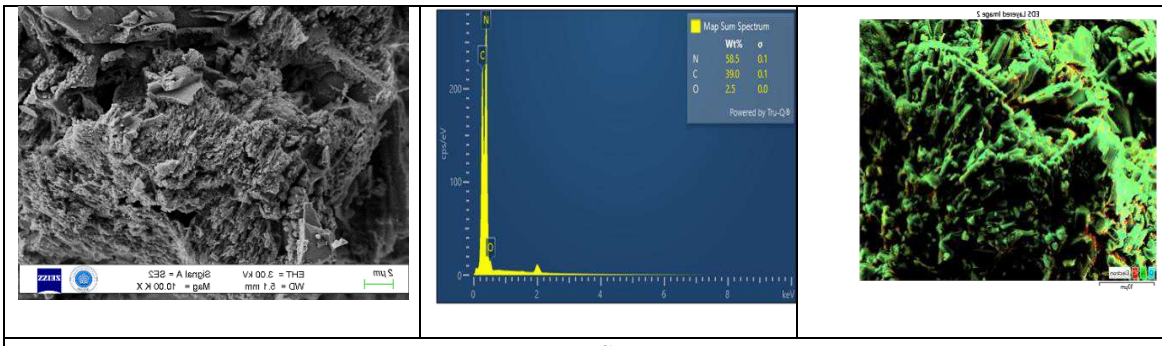


Fig 5(a). Point of zero charge (pHpzc) of g-C_3N_4 @ZIF-8	Fig 5(b) X-ray Photoelectron Spectroscopy (XPS) Analysis of g-C_3N_4@ZIF-8

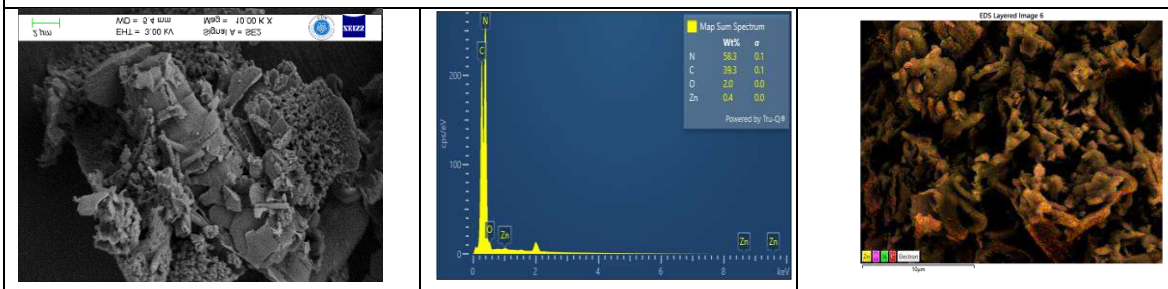
The pHpzc value, which means the pH value of the solution at which the total charge on the surface of the nanoparticles is zero (neutral), was calculated (Gatabi et al., 2016). The common drift method (or Corman Drift Method) was used to determine the pHpzc value, which means the zero charge point or isoelectric point. For this method, five different 20 ml, 0.01 M sodium chloride (NaCl) solutions were prepared and the pH values of the solutions were adjusted to 2, 4, 6, 8, and 10 using 0.1 M NaOH and 0.1 M nitric acid (HNO_3). 2 mg of particles were put into each solution and the resulting suspensions were stirred for 24 hours at 25 ºC with a shaking speed of 150 rpm. At the end of 24 hours, the particles were separated from the suspensions and the final pH (*PH(fin)*) values were measured (Pereira et al., 2019). The ΔpH values were plotted against the initial pH (pH_0) values (Figure 5 (a)). The pHpzc value of the nanoparticle was found to be 7.485.

Figure 5 (b) shows the XPS spectrum of g-C_3N_4@ZIF-8. As shown in the full scan spectrum in Figure, Zn, C, N, and O elements were detected, and the O 1s peak can probably be attributed to the adsorption of CO_2 and H_2O molecules on the surface of the sample. The peak at 284.6 eV in the C 1s spectrum represents sp^2 hybridized C–C bonds, and the peak around 288.1 eV represents N–C=N bonds in the g-C_3N_4 structure (Yang et al., 2023). The shift of the C 1s peak to 287.8 eV with the formation of the composite indicates electron transfer and chemical interaction between ZIF-8 and g-C_3N_4. The peaks at 398.5 and 400.0 eV in the N 1s region represent C=N–C bonds and terminal –NH groups, respectively (Yang et al., 2023). The peaks at 1021.7 eV Zn $2p_{3/2}$ and 1044.8 eV Zn $2p_{1/2}$ in the Zn 2p spectrum confirm the presence of Zn^{2+} ions and the preservation of the ZIF-8 structure in the composite (Sun et al., 2024). The approximately 0.1 eV increase in C 1s and N 1s, and the 0.2 eV decrease in Zn 2p, indicate a redistribution of surface electron density(Zheng et al., 2021). Small shifts in binding energies indicate strong interactions between the components and a redistribution of surface electron density. These results confirm that g-C_3N_4 successfully composites with ZIF-8 while maintaining its structural integrity.



g-C₃N₄

Fig 6(a). SEM images of g-C_3N_4, elemental mapping image of O, N and C, and EDX spectrum of g-C_3N_4



g-C₃N₄@ZIF-8

Fig 6(b). SEM images of g-C_3N_4@ZIF-8, elemental mapping image of C, N, O and Zn, and EDX spectrum of g-C_3N_4@ZIF-8

The surface images of g-C_3N_4 and g-C_3N_4@ZIF-8 molecules were detected by SEM. Figure 6(a-b) exhibit the solid sheet-like structures resulting from g-C_3N_4. Nanoscale layers are stacked on top of each other, exhibiting a specific curvature. The structure is generally porous, with spaces between the layers. This porous architecture facilitates the access of molecules to the surface during catalytic reactions, increasing their efficiency (Nguyen et al., 2020). Aggregates consisting of fewer sheets and larger stacked structures can be observed in g-C_3N_4@ZIF-8, confirming the successful assembly of g-C_3N_4 and ZIF-8 molecule. On the g-C_3N_4@ZIF-8 surface, particles are uniformly and homogeneously distributed. It was also observed that the particles tend to accumulate between the layers (Golami et al., 2024).The ZIF-8 additive transformed the layer structure of g-C_3N_4 into a tighter, more regular, and particulate morphology. The elemental composition of the g-C_3N_4@ZIF-8 nanocomposite doped with 0.1 wt% ZIF-8 was investigated in detail. EDS mapping images for both samples showed the distribution of surface elements of C, N, O and Zn. Zn is not present in g-C_3N_4 molecule, while it is present in g-C_3N_4@ZIF-8 composite containing ZIF-8. The analyses revealed that ZIF-8 crystals are uniformly distributed on the layered structure of g-C_3N_4, resulting in a more complex morphology. The absence of any impurity elements indicates that the material is homogeneously formed and has high purity.

289

290 3.2. Catalytic experiment results

291 g-C_3N_4@ZIF-8 nanoparticles were selected for the catalytic removal of ARS and KEP in aqueous solution. 25
292 mg/L stock solutions of ARS and KEP were prepared separately. The degradation spectra of these solutions were
293 recorded using UV-Vis in the scanning range of 200-800 nm at ambient temperature (25±1 °C). The degradation
294 reaction of ARS was scanned at 524 nm on a UV-Vis spectrophotometer, while KEP was scanned at a maximum
295 wavelength of 260 nm. The catalytic effects of NPs on ARS and KEP removal were optimized by the factors of
296 pH, concentration, particle dose, and $NaBH_4$ amount. All kinetic studies reported in this study were performed
297 under normal conditions. Catalyzed reaction rates were measured by monitoring the change in catalytic activity
298 with time for both KEP and ARS. Degradation experiments of the ARS and KEP in question were carried out in
299 the presence of $NaBH_4$ used as a reductant, and the degradation times were monitored under UV-Vis
300 (Ahmaruzzaman et al., 2019). To study the effect of g-C_3N_4@ZIF-8 on ARS and KEP removal, a certain amount
301 of NPs ranging from 1 to 3 mg were added to 2 mL of solutions containing 25 mg/L ARS or KEP, respectively.
302 To study the pH effect of dye and drug, g-C_3N_4@ZIF-8 NP catalysts at different pH values were added to 2 mL of
303 aqueous solutions containing 25 mg/L ARS or 25 mg/L KEP. To determine the effect of contaminant
304 concentration, catalysis was performed by adding 2 mg of C_3N_4@ZIF-8 particles at an initial concentration of 10-
305 25 mg/L ARS and 10-25 mg/L KEP.
306 In the study, it was observed that sodium borohydride facilitated the reduction of ARS and KEP, however, this
307 process was not completely achieved when the degradation was carried out without the use of g-C_3N_4@ZIF-8. To
308 evaluate the catalytic activity of g-C_3N_4@ZIF-8, its catalytic reactions with ARS and KEP compounds were
309 studied under different conditions in the presence and absence of $NaBH_4$. Under the same experimental conditions,
310 only 22.0% ARS and 19.0% KEP were removed by g-C_3N_4@ZIF-8 NPs in the absence of $NaBH_4$. The addition
311 of g-C_3N_4@ZIF-8 as a catalyst provided an alternative pathway with lower activation energy for the desired
312 reduction reaction, reducing the kinetic barrier and making the reaction more favorable. It was thought that g-
313 C_3N_4@ZIF-8 provided a suitable surface for the interaction of KEP and ARS particles with borohydride ions
314 (BH_4^-) leading to the formation of degradation products. These nanoparticles kinetically facilitated the degradation
315 of KEP and ARS, resulting in complete reduction in a short time. According to this result, g-C_3N_4@ZIF-8 alone
316 does not have catalytic ability, but when used with $NaBH_4$, the removal efficiency and rate of ARS or KEP
317 molecules were significantly increased. This indicates that g-C_3N_4@ZIF-8 NPs have a strong catalytic ability to

remove ARS or KEP in the presence of $NaBH_4$. Catalytic experiments were completed with the removal efficiency reaching 84.5% after 50 min for ARS and 99.4% after 20 min for KEP.

As a result, g-C_3N_4@ZIF-8 NPs showed excellent catalytic activity for AR and KEP removal with higher removal efficiency and faster reaction rate. It is known that this is mainly due to ZIF-8 in the g-C_3N_4@ZIF-8 composite.

3.2.1 Catalytic Degradation of KEP and ARS under Different Experimental Conditions

g-C_3N_4@ZIF-8 as a catalyst has been extensively investigated for its ability to degrade KEP and ARS, which lead to their pollution by being released into water bodies. For the KEP degradation experiments, 4 mL solution was prepared from 1 mg catalyst and 2 mL of 25 mg/L ketoprofen solution and 1.6 mM $NaBH_4$ solution. For catalysis experiments, firstly, as a 0th min measurement, UV-Vis spectroscopy was scanned in the range of 200-800 cm^{-1} without adding catalyst and then, with periodic measurements every 5 minutes by adding catalyst, ketoprofen change in the medium was monitored (Figure 8(a) and 9(a)). Before the measurements, the samples were centrifuged (13,000 rpm min^{-1}) to remove catalyst particles.

The catalytic reduction reaction of KEP and ARS with g-C_3N_4@ZIF-8 can be explained by the electron transfer effect. ZIF-8 facilitates electron transfer between donors and receptors, allowing the transfer of electrons from donors ($BH4^-$) to acceptors, KEP and ARS, via a redox mechanism. In the catalytic reaction, g-C_3N_4@ZIF-8 is used with $NaBH_4$, a reducing agent, to facilitate the degradation of KEP and ARS. The basic mechanism of the degradation is that g-C_3N_4@ZIF-8 is used as an electron relay, allowing electrons to be transferred from the BH_4-ion (donor B_2H_4/BH_4) to the acceptor (KEP and ARS), resulting in a reduction reaction. The BH_4^- ion is adsorbed on the surface of the NPs, which leads to electron transfer from the BH_4^- ion to the dye via the NPs. g-C_3N_4@ZIF-8 offers a sustainable and effective method for the permanent removal of KEP and ARS from water via catalysis. In this detailed study, g-C_3N_4@ZIF-8 has been proven to be useful in the degradation of KEP and ARS in a short time.

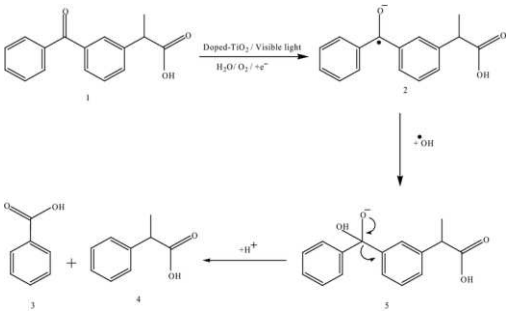


Fig. 7(a). Possible degradation pathways of KEP

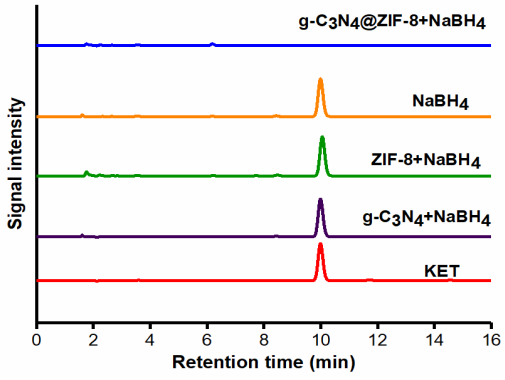


Fig. 7(b). Initial and post-process HPLC chromatograms of KEP solutions used in the KEP removal experiment with g-C_3N_4@ZIF-8 under optimum conditions

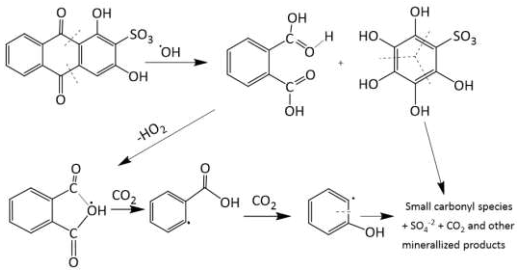


Fig. 7(c). Possible degradation pathways of ARS [53].

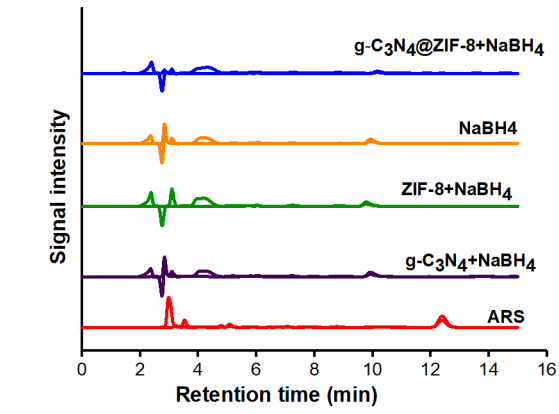


Fig. 7(d). Initial and post-process HPLC chromatograms of ARS solutions used in the ARS removal experiment with g-C_3N_4@ZIF-8 under optimum conditions

Sodium borohydride dissociates in water into Na^+ and BH_4^{-1} ions. The BH_4^{-1} ions serve as a source of both the hydride ions present on the surface of the g-C_3N_4@ZIF-8 nanoparticles and the hydride ions surrounding the ARS and KEP molecules. Hydrogen is released from the BH_4^{-1} ions on the catalyst surface, and electrons are transferred to the catalyst. g-C_3N_4@ZIF-8 acquires electrons and activates the bonds between the ARS and KEP molecules. Conjugation weakens and breaks the X-bond between the ARS and KEP molecules. In the first step of the reaction, –N—N- is converted to a nitrogen–nitrogen single bond, which is then broken from the –NH–NH- bond, making the dye lighter and eventually colorless. After the reaction is complete, the product leaves the metal surface and

diffuses. The extent of decomposition of both AR (max. 524 nm) and KEP (max. 260 nm) in aqueous solution was determined by UV spectrometry at overlapping wavelengths due to the π-π* and n-π* transitions and the R* band. In the KEP removal study carried out using g-C_3N_4@ZIF-8, HPLC chromatograms of the solutions obtained after catalyst-free degradation ($NaBH_4$) and catalytic degradation (g-C_3N_4 + $NaBH_4$, ZIF-8 + $NaBH_4$, g-C_3N_4@ZIF-8 + $NaBH_4$) processes applied to KEP solution at a concentration of 25 mg/L were recorded at 260 nm wavelength Figure 7(b). In the initial chromatogram of the KEP solution recorded at 260 nm (Fig.7(b)(red)), the peak observed at approximately 10 minutes confirms the presence of KEP molecules (Shaalan et al., 2013). No significant change was observed in this characteristic KEP peak in the control experiment without catalyst (yellow) and in the unmodified systems (purple and yellow). In contrast, the KEP peak at 10 minutes was completely lost in the degradation process in the presence of g-C_3N_4@ZIF-8 catalyst. The disappearance of the characteristic peak indicates that the KEP molecules are structurally damaged. Furthermore, the new peak observed at approximately 2 minutes in the catalytic degradation chromatograms (260 nm) indicates that KEP is converted into degradation products.

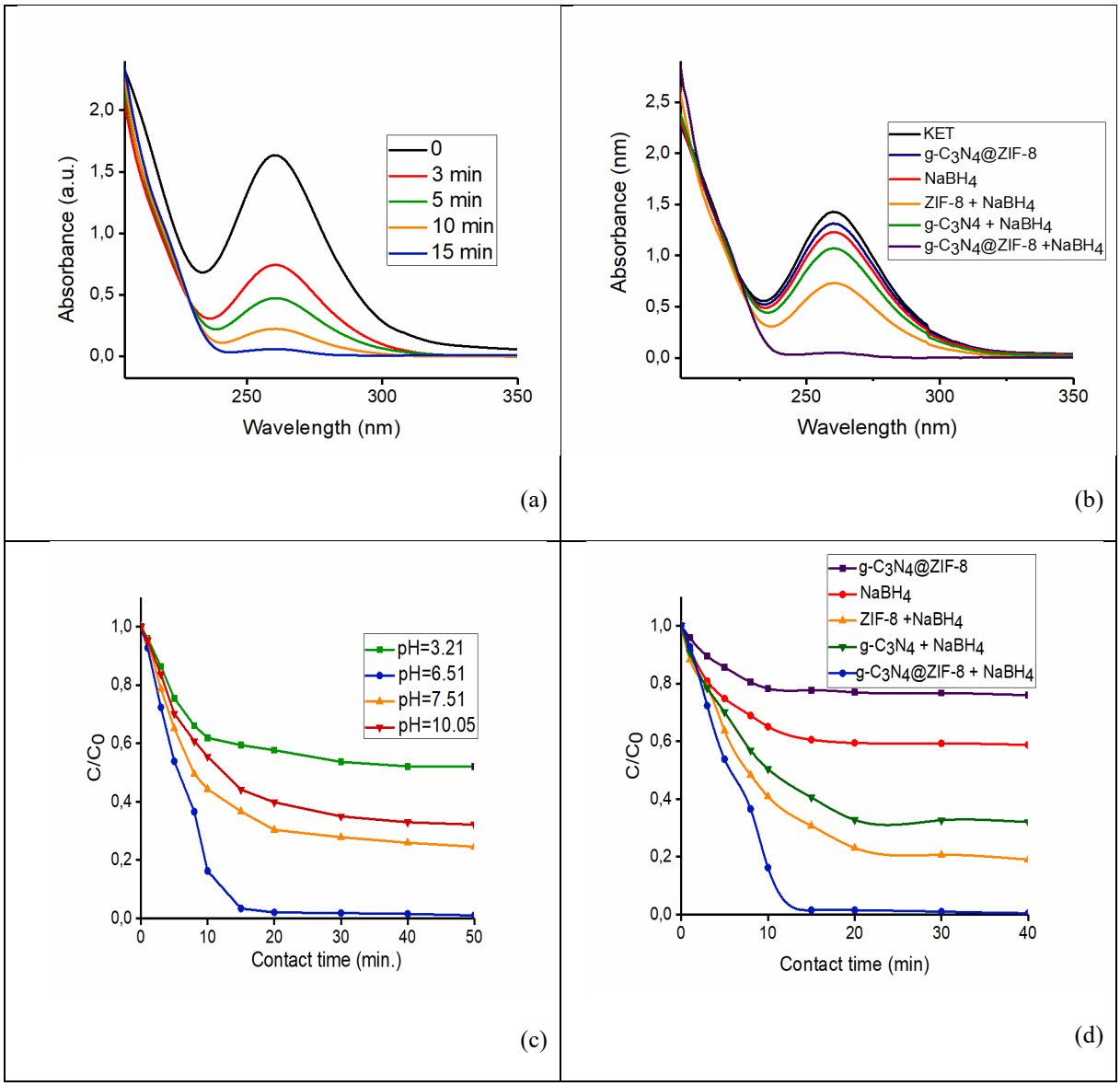
KEP was reduced by electron/hydride transfer mediated by BH_4^- adsorbed onto the g-C_3N_4@ZIF-8 surface in the presence of $NaBH_4$. Reduction or decarboxylation of the carboxyl group may have occurred during this process (Borsarelli et al., 2000). It is thought that benzophenone-like intermediates are then formed via hydroxylation or hydrogenation of the aromatic ring (Djouadi et al., 2018). The high surface area and active centers of g-C_3N_4@ZIF-8 accelerated this transformation by facilitating electron transfer. The appearance of new peaks at short retention times in HPLC analysis indicates the formation of more polar and smaller molecules. Thus, it can be concluded that KEP follows a multistage degradation pathway, with the cyclic structure breaking through reduced derivatives (Li et al. 2017).

In the initial chromatogram of a 25 mg/L ARS solution obtained at 524 nm (Figure 7(d), (red)), characteristic peaks specific to the ARS molecule were observed at 3.1 and 11.4 minutes (Khamis et al., 2020). No significant change was observed in these peaks in the catalyst-free control experiments (yellow) and in the unmodified systems (purple and yellow). As a result of the catalytic degradation in the presence of the g-C_3N_4@ZIF-8 catalyst, the peak at 11.4 minutes completely disappeared, and the peak height at 3.1 minutes decreased. The simultaneous appearance of a new peak around 4.2 minutes indicates that the ARS molecule has undergone structural degradation and new intermediates have been formed.

The appearance of new peaks in the chromatogram at the end of the degradation process indicates that the dye has transformed into more polar and lower molecular weight intermediates or end products. These new peaks are

thought to correspond to derivative compounds formed as a result of reactions such as partial opening of aromatic rings and conversion of sulfonate groups.

In this study, ketoprofen was tried to be removed with the g-C_3N_4@ZIF-8 catalyst at different pH values, pollutant concentrations, $NaBH_4$ concentrations, catalyst amount and even without using a catalyst. When optimum conditions were created with the g-C_3N_4@ZIF-8 composite, ketoprofen degradation of up to 99.4% was achieved. To determine the effect of pH on ketoprofen removal, catalytic degradation processes were applied to ketoprofen solutions with pHs of 3.21, 6.51, 7.51, and 10.05. In addition, the effects of catalyst amount (1, 2, 3 mg), KEP concentrations (15-30 mg/L), and $NaBH_4$ concentration (0.5-1.6 mM) on KEP removal were investigated and the results are presented in Figure 8 (a-h).



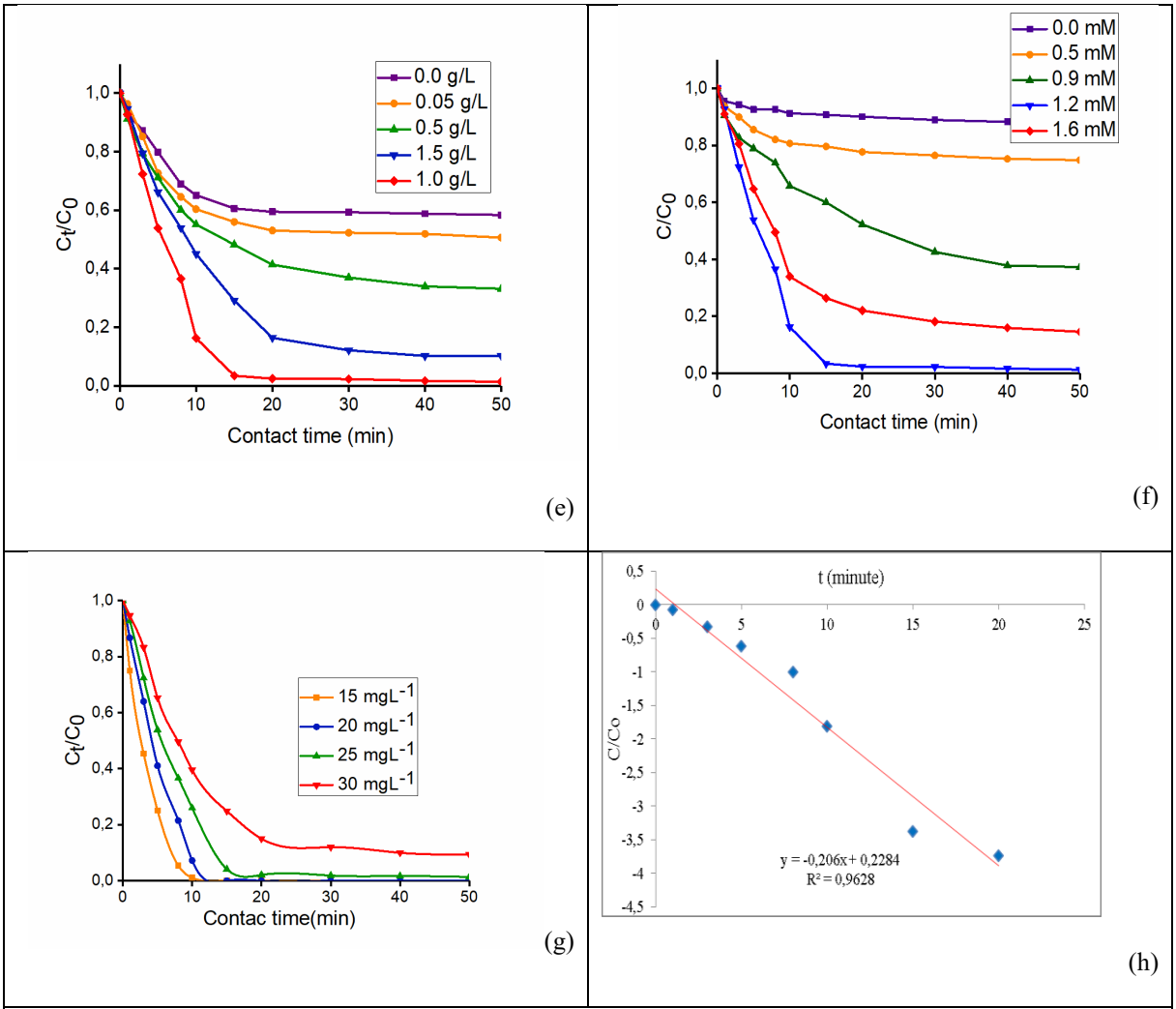


Fig. 8 (a). UV-Vis spectrum of chemical catalytic removal of KEP (*Experimental conditions: $NaBH_4$ concentration 1.2 mM, g-C_3N_4 @ZIF-8 dosage 1.0 g/L, initial KEP concentration 25 mg/L*)., (b) UV-Vis spectrum of chemical catalytic removal of KEP under different conditions (Experimental conditions: $NaBH_4$ concentration 1.2 mM, g-C_3N_4 @ZIF-8 dosage 1.0 g/L, initial KEP concentration 25 ppm, 15 min), (c) Effect of pH on KEP removal using g-C_3N_4@ZIF-8 nanoparticle *(Experimental conditions; 1.0 g/L g-C_3N_4@ZIF-8, 25 mg/L KEP and 1.2 mM $NaBH_4$),* (d): Comparison of chemical catalytic degradation experiments of KEP under different experimental conditions *(Experimental parameters: pH 6.56, $NaBH_4$ concentration 0.5 mM, g-C_3N_4 @ZIF-8 dosage 1.0 g/L, initial concentration 25 ppm).*, (e). Effect of g-C_3N_4 @ZIF-8 dosage on KEP degradation *(Experimental parameters: pH=6.51, 25 mg/L KEP and 1.2 mM $NaBH_4$),*(f). Effect of $NaBH_4$ concentration on the removal of ketoprofen via catalytic degradation *(Experiment parameters: pH 6.51, g-C_3N_4 @ZIF-8 dosage 1.0 g/L, KEP concentration 25 mg/L).*, (g) *Effect of drug concentration on KEP removal using g-C_3N_4@ZIF-8 (Experimental conditions; 1.0 g/L g-C_3N_4@ZIF-8, pH= 6.51 and 1.2 mM $NaBH_4$),* (h) Catalytic degradation and First-order kinetics curves of KEP with g-C_3N_4@ZIF-8.

Catalytic performance study was carried out using ARS. For this purpose, ARS removal was examined under conditions with and without the use of catalyst. Figure 9 shows the catalytic degradation curves of ARS. In the study, ARS was degraded up to 84.5% under optimum conditions with g-C_3N_4@ZIF-8. Similar to the KEP study, in order to determine the effects of different parameters on ARS removal, different pHs (3.12, 6.55, 7.45 and

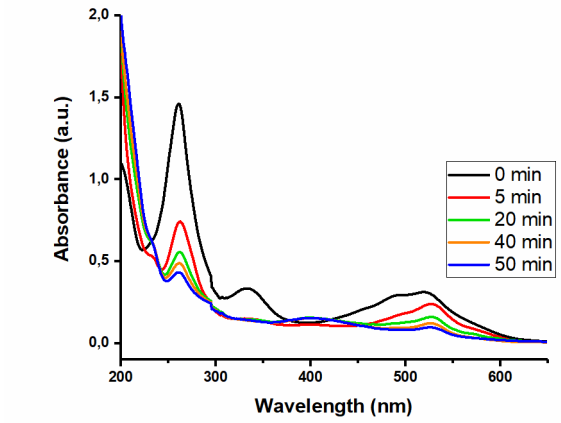
10.23), catalyst amount (0.5, 1.0, 1.5 mg) and $NaBH_4$ concentration (2.0-2.8 mM) were studied and the results are presented in Figure 9(a-h).

The effect of catalyst amount on the removal of KEP and AR is shown in Figure 8(g) and Figure 9(g). For both pollutants, higher amount of g-C_3N_4@ZIF-8 NPs used means higher catalytic efficiency and reaction rate. As shown in the figures, the removal efficiency of KEP was 34.1% in 50 min after the addition of 1 mg g-C_3N_4@ZIF-8 NPs, while it increased to 81.5% at the dosage of 2 mg g-C_3N_4@ZIF-8 NPs. Similarly, for ARS, the catalytic efficiency increased from 5% to 10% when the dosage was increased from 1 mg to 2 mg. The increase in the amount of g-C_3N_4@ZIF-8 NPs increases the surface area of the catalyst, enabling the transfer of active hydrogens and electrons to the target pollutants Therefore, the removal efficiency of the pollutants increased greatly with the increase of the active surface area of the catalyst and the reaction time was shortened. However, the removal rate and time of KEP and ARS did not change significantly when the amount of g-C_3N_4@ZIF-8 NPs exceeded 3 mg for both pollutants. This may be due to the limited number of electrons produced by a certain amount of $NaBH_4$, which is the reductant in the medium. Moreover, higher amount of catalyst can reduce the surface area by agglomerate formation of catalyst particles. This is because at higher doses the catalyst aggregates, leading to a decrease in the number of active sites responsible for catalytic reactions. Therefore, the optimum dosage of catalytic material was kept constant at 2 mg for each experiment.

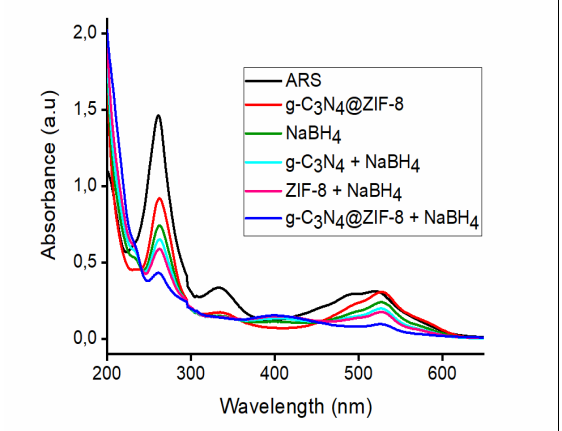
The effect of pH on the catalytic efficiency of g-C_3N_4@ZIF-8 NPs for the degradation of KEP and ARS in the presence of $NaBH_4$ was studied. The degradation rate of KEP and ARS was found to be higher in neutral pH environments compared to basic or acidic environments. It was also seen that degradation was higher in basic environments compared to acidic environments for both substances. It is thought that this change in the degradation rate is due to the pH affecting the chemical structure of both the catalyst and KEP and ARS, and also due to structural changes in the catalyst depending on the pH.

As shown in Figure 8(c) and Figure 9(c), when the solution pH was varied between 3.12 and 10.23, the removal efficiency of KEP was found to be between 38.9% and 99.4% after every 50 min of reaction time, and between 20.2% and 84.5% for ARS after a 70-minute reaction time.

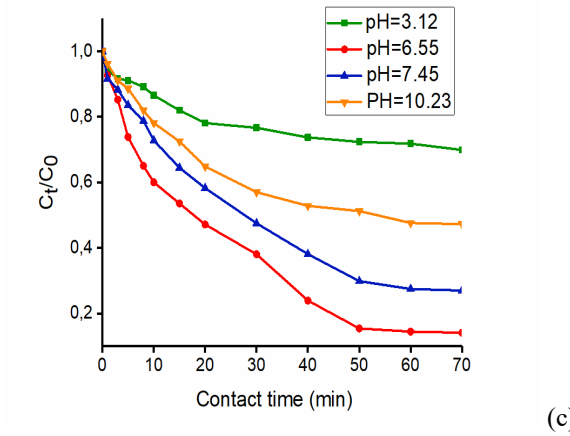
The study showed that g-C_3N_4@ZIF-8 NPs could be used to remove both pollutants in the specified pH range and their removal was dependent on the solution pH. It was observed that high removal efficiencies were obtained at pH values of about 7.0, which is close to the neutral pH value for KEP and ARS. The pH study indicated that g-C_3N_4@ZIF-8 NPs could effectively remove pollutants under near-neutral conditions.


Absorbance (a.u.)
Wavelength (nm)
0 min
5 min
20 min
40 min
50 min

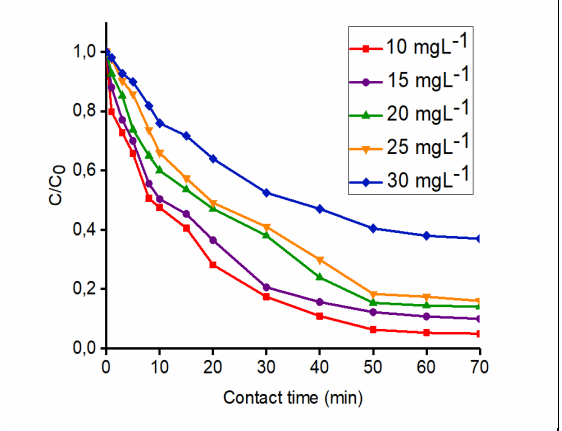
(a)


Absorbance (a.u.)
Wavelength (nm)
ARS
g-C3N4@ZIF-8
NaBH4
g-C3N4 + NaBH4
ZIF-8 + NaBH4
g-C3N4@ZIF-8 + NaBH4

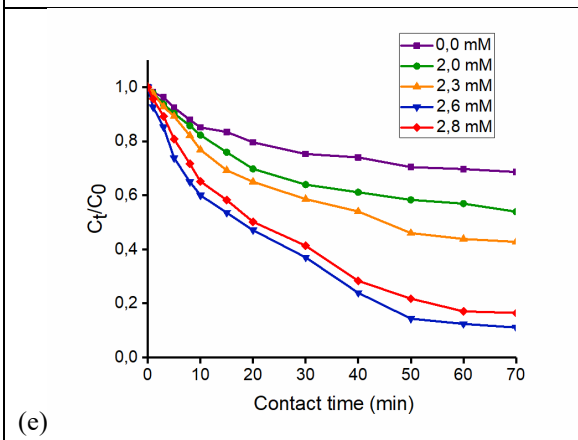
(b)


Ct/C0
Contact time (min)
pH=3.12
pH=6.55
pH=7.45
PH=10.23

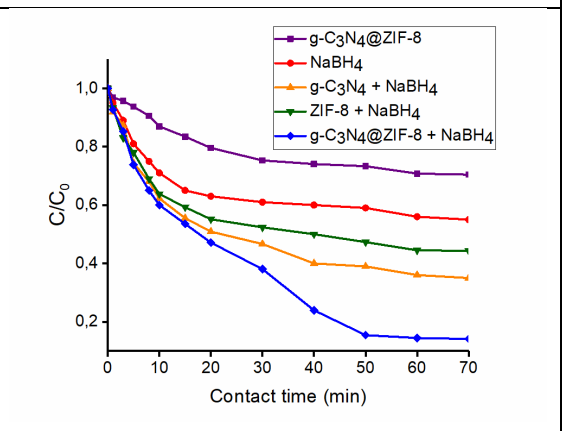
(c)


C/C0
Contact time (min)
10 mgL-1
15 mgL-1
20 mgL-1
25 mgL-1
30 mgL-1

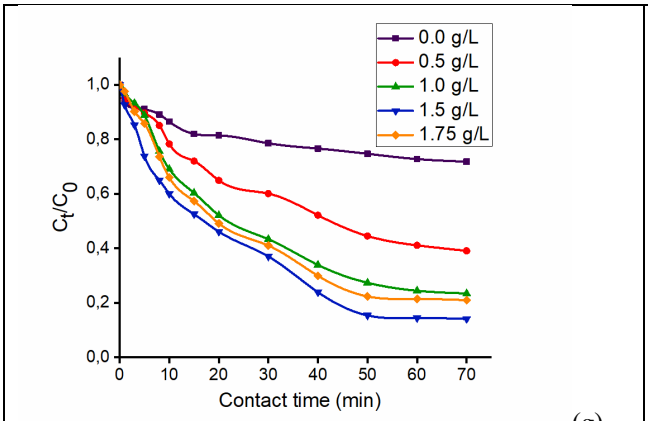
(d)


Ct/C0
Contact time (min)
0,0 mM
2,0 mM
2,3 mM
2,6 mM
2,8 mM

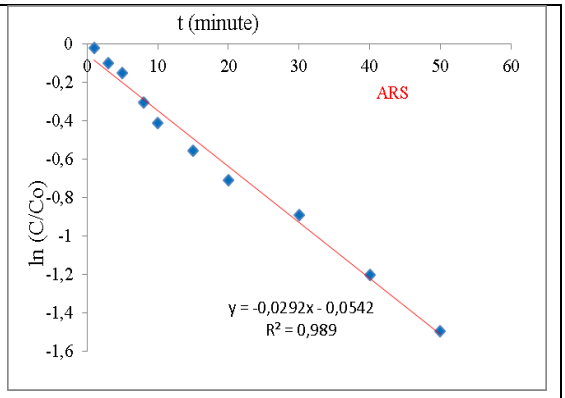
(e)


C/C0
Contact time (min)
g-C3N4@ZIF-8
NaBH4
g-C3N4 + NaBH4
ZIF-8 + NaBH4
g-C3N4@ZIF-8 + NaBH4

(f)



(g)



(h)

Fig. 9 (a). UV-Vis spectrum of chemical catalytic removal of ARS (*Experimental conditions* 1.5 g/L g-C_3N_4@ZIF-8 ve 2.6 Mm $NaBH_4$ pH=6,55), (b) UV-Vis spectrum of chemical catalytic removal of ARS under different conditions (Experimental conditions: $NaBH_4$ concentration 1.6 mM, g-C_3N_4@ZIF-8 dosage 1.5 g/L, initial ARS concentration 20 g/L, 70 min). (c) Effect of pH on ARS removal using g-C_3N_4@ZIF-8 nanoparticle *(Experimental conditions; 1.5 g/L g-C_3N_4@ZIF-8, 20 mg/L ARS ve 2.6 mM $NaBH_4$)*, (d) Effect of drug concentration on ARS removal using g-C_3N_4@ZIF-*8 (Experimental conditions; 1.5 g/L g-C_3N_4@ZIF-8, pH= 6.55 and 2.6 mM $NaBH_4$).*, (e) Effect of NaBH4 amount on ARS dye removal using g-C3N4@ZIF-8 nanoparticle (experimental conditions; 1.5 g/L g-C3N4@ZIF-8 20 mg /L ARS and pH=6.55), (f) Comparison of chemical catalytic degradation experiments of KEP under different experimental conditions *(Experimental parameters: pH 6.56, $NaBH_4$ concentration 1.5 mM, g-C_3N_4 @ZIF-8 dosage 1.5 g/L, initial concentration 20 mg/L).*, (g) Effect of particle amount on ARS dye removal using g-C_3N_4@ZIF-8 nanoparticle (experimental conditions; pH=6, 45, 20 mg/L ARS and 2.6 mM NaBH4), (h) Catalytic degradation and First-order kinetics curves of ARS with g-C_3N_4@ZIF-8

3.2.2 Kinetics Studies of ARS and KEP

The kinetic parameters of the degradation process for KEP and ARS were calculated using the pseudo-first-order reaction model. In the whole reaction process, since the $NaBH_4$ concentration was much higher than the pollutant concentrations, it was considered as a constant and the kinetic constants for KEP and ARS were calculated using the pseudo-first-order kinetic equation. For this purpose, a straight line was obtained by plotting $ln[C_0/C_t]$ against time*(t)*, confirming that the reduction process follows the pseudo-first-order reaction kinetics. The results are given graphically in Figure 8-9 (h). The kinetic equation of this catalytic reduction reaction can be given as $ln[C_0/C_t] = -kt$ (Prasanna et al., 2024). Here, k is the apparent first-order rate constant (min^{-1}) and t is the reaction time, C_t and C_o are the KEP and ARS concentrations at time t and 0, respectively. The reaction rate constants k were calculated for the g-C_3N_4@ZIF-8 in which KEP and ARS were degraded and k of g-C_3N_4@ZIF-8 for KEP and ARS were found to be 0.206 min^{-1} and 0.0292 min^{-1}, respectively.

4. Results and discussion

In this study, g-C_3N_4 containing NP was successfully synthesized using MOF derivative ZIF-8. g-C_3N_4@ZIF-8 NPs were characterized in detail both structurally and superficially. Then, g-C_3N_4@ZIF-8 NPs were successfully used as a catalyst for the catalytic degradation of KEP, one of the most widely used active pharmaceutical ingredients, and ARS dye, which is also widely used. The effects of pH, $NaBH_4$ amount and impurity concentration on the degradation were studied and the catalytic degradation efficiency of these two substances under optimum conditions was found to be 99.4% (KEP) and 84.5% (ARS). Possible degradation mechanisms were suggested using HPLC.

Acknowledge

The authors would like to thank Selcuk University and the Turkish Academy of Sciences (TÜBA) for their support. The presented work was financially supported by Selcuk University Scientific Research Projects (Grant Number: 22211017), the European Union's Horizon 2020 research and innovation program "Strengthening the Scientific Excellence of Selcuk University in Engineered Surfaces and Films for Emerging Technologies" project (GA: 952289).

Author Contributions

Ayşe Bayrak: Synthesis, characterization, and catalytic degradation; Sevde Demir: ZIF-8 synthesis; Hakan Erer: ZIF-8 synthesis and characterization, methodology; Ilkay Hilal Gubbuk: Research, Writing, Evaluation; Mustafa Ersoz: Conceptualization, Data Curation, Research.

Declarations

Ethical Approval: Not Applicable.

Funding: No funding support is available.

Availability of data and materials: All raw data files for XRD, UV(DRS), and XPS spectra are available upon request.

Consent for Publication: The publication of this article has been approved by all co-authors.

Conflict of Interest: The authors declare that they have no known conflicts of interest or personal relationships that could have appeared to influence this work.

References

Abed HH, Ammar SH. Case Studies in Chemical and Environmental Engineering.

Ahmaruzzaman M, Mohanta D, Nath A. (2019) Environmentally benign fabrication of SnO_2-CNT nanohybrids and their multifunctional efficiency as an adsorbent, catalyst and antimicrobial agent for water decontamination. Sci. Rep. 9(1):12935.

Ahmed S, Khan FSA, Mubarak NM, Khalid M, Tan YH, Mazari SA, et al. (2021) Emerging pollutants and their removal using visible-light responsive photocatalysis–a comprehensive review. J Environ. Chem. Eng. 9(6):106643.

Asadi A, Daglioglu N, Hasani T, Farhadian N. (2022) Construction of Mg-doped ZnO/g-C_3N_4@ ZIF-8 multi-component catalyst with superior catalytic performance for the degradation of illicit drug under visible light. Colloids and Surfaces A: Physicochemical and Engineering Aspects.650:129536.

Atzeni F, Masala IF, Bagnasco M, Lanata L, Mantelli F, Sarzi-Puttini P. (2021) Comparison of efficacy of ketoprofen and ibuprofen in treating pain in patients with rheumatoid arthritis: a systematic review and meta-analysis. Pain and Therapy.10(1):577-88.

Bag PP, Singh GP, Singha S, Roymahapatra G. (2020) Synthesis of metal-organic frameworks (MOFs) and their biological, catalytic and energetic application: a mini review. Eng. Sci. 13(19):1-10.

Banerjee R, Furukawa H, Britt D, Knobler C, O'Keeffe M, Yaghi OM. (2009) Control of pore size and functionality in isoreticular zeolitic imidazolate frameworks and their carbon dioxide selective capture properties. J Am. Chem. Soc.131(11):3875-7.

Banerjee R, Phan A, Wang B, Knobler C, Furukawa H, O'Keeffe M, et al. (2008) High-throughput synthesis of zeolitic imidazolate frameworks and application to CO_2 capture. Science.319(5865):939-43.

Borsarelli CD, Braslavsky SE, Sortino S, Marconi G, Monti S. (2000) Photodecarboxylation of Ketoprofen in Aqueous Solution. A Time-resolved Laser-induced Optoacoustic Study¶. Photochem. Photobiol. 72(2):163-71.

Chen B, Yang Z, Zhu Y, Xia Y. (2014) Zeolitic imidazolate framework materials: recent progress in synthesis and applications. J Mater. Chem. A.2(40):16811-31.

Chirra S, Wang L-F, Aggarwal H, Tsai M-F, Soorian SS, Siliveri S, et al. (2021) Rapid synthesis of a novel nano-crystalline mesoporous faujasite type metal-organic framework, ZIF-8 catalyst, its detailed characterization, and NaBH4 assisted, enhanced catalytic Rhodamine B degradation. Mater. Today Commun. 26:101993.

501 Djouadi L, Khalaf H, Boukhatem H, Boutoumi H, Kezzime A, Santaballa JA, et al. (2018) Degradation of aqueous
502 ketoprofen by heterogeneous photocatalysis using Bi_2S_3/TiO_2–Montmorillonite nanocomposites under
503 simulated solar irradiation. Appl Clay Sci. 166:27-37.
504 Gatabi MP, Moghaddam HM, Ghorbani M. (2016) Point of zero charge of maghemite decorated multiwalled
505 carbon nanotubes fabricated by chemical precipitation method. J Mol. Liq. 216:117-25.
506 Gautam RK, Mudhoo A, Chattopadhyaya MC. (2013) Kinetic, equilibrium, thermodynamic studies and
507 spectroscopic analysis of Alizarin Red S removal by mustard husk. J Environ. Chem. Eng. 1(4):1283-91.
508 Gholivand MB, Yamini Y, Dayeni M, Seidi S, Tahmasebi E. (2015) Adsorptive removal of alizarin red-S and
509 alizarin yellow GG from aqueous solutions using polypyrrole-coated magnetic nanoparticles. J Environ.
510 Chem. Eng.3(1):529-40.
511 Golami Ghiaci Z, Rafiee Z. (2024) g-C_3N_4/Fe_2O_3/ZIF-8 catalyst for the synthesis of polyhydroquinoline
512 derivatives via Hantzsch reaction. Res. Chem. Intermediat. 50(3):1161-75.
513 Guo T, Wang K, Zhang G, Wu X. (2019) A novel α-Fe2O3@ g-C3N4 catalyst: synthesis derived from Fe-based
514 MOF and its superior photo-Fenton performance. Appl. Surf. Sci. 469:331-9.
515 He H, Liang B, Lin S, Chen Y, Zhang X, Liang S-X. (2024) Photodegradation of oxytetracycline hydrochloride
516 by Z-scheme g-C_3N_4@ MIL-101 (Fe) heterojunction: Experimental optimization, mechanism evaluation
517 and practical application. J Environ. Chem. Eng.12(2):112018.
518 Jomekian A, Bazooyar B, Esmaeilzadeh J, Behbahani RM. (2020) Highly CO_2 selective chitosan/g-C3N4/ZIF-8
519 membrane on polyethersulfone microporous substrate. Sep. Purif. Tech. 236:116307.
520 Karimi-Maleh H, Darabi R, Shabani-Nooshabadi M, Baghayeri M, Karimi F, Rouhi J, et al. (2022) Determination
521 of D&C Red 33 and Patent Blue V Azo dyes using an impressive electrochemical sensor based on carbon
522 paste electrode modified with ZIF-8/g-C_3N_4/Co and ionic liquid in mouthwash and toothpaste as real
523 samples. Food Chem. Toxicol. 162:112907.
524 Khamis MI, Ibrahim TH, Jumean FH, Sara ZA, Atallah BA. (2020) Cyclic sequential removal of alizarin red S
525 dye and Cr (VI) ions using wool as a low-cost adsorbent. Processes.8(5):556.
526 Li J, Ma Ly, Li Ls, Xu L. (2017) Photodegradation kinetics, transformation, and toxicity prediction of ketoprofen,
527 carprofen, and diclofenac acid in aqueous solutions. Environ. Toxicol. Chem. 36(12):3232-9.
528 Li T, Zhang W, Zhai S, Gao G, Ding J, Zhang W, et al. (2018) Efficient removal of nickel (II) from high salinity
529 wastewater by a novel PAA/ZIF-8/PVDF hybrid ultrafiltration membrane. Water res. 143:87-98.

Li X, Liu H, Meng S, Wang L. Three birds with one stone: (2024) ZIF-8@ g-C_3N_4 nanosheets simultaneously enhance barrier property, active protection and UV aging resistance of epoxy coatings. Sep. Purif. Tech.:129722.

Li X, Lv X, Ding S, Huang L, Wei Z. (2022) Mixed matrix membranes containing composite nanosheets with three-dimensional nanopores for efficient CO2 separation. Inter. J Greenhouse Gas Control.117:103658.

Lin Y, Wang M, Ji L, Li S, Zhang Y, Wei L, et al. (2024) Catalytic reduction of p-nitrophenol by g-C3N4/$CuFe_2O_4$ magnetic nanocomposites. Opt. Mater.157:116070.

Li Z, Zhu J, Teng P, Yang X, Wang Y, Gao S, et al. (2022) Preparation of flexible PAN–C3N4–ZIF-8 photocatalytic nanofibers and visible light catalytic properties. Opt. Mater.132:112762.

Liu X, Zhang J, Dong Y, Li H, Xia Y, Wang H. (2018) A facile approach for the synthesis of Z-scheme photocatalyst ZIF-8/gC_3N_4 with highly enhanced photocatalytic activity under simulated sunlight. New J Chem. 42(14):12180-7.

Lu G, Li S, Guo Z, Farha OK, Hauser BG, Qi X, et al. (2012) Imparting functionality to a metal–organic framework material by controlled nanoparticle encapsulation. Nat. Chem. 4(4):310-6.

Ma K, Wang N, Wang C, An Q-F. (2021) Freezing assisted in situ growth of nano-confined ZIF-8 composite membrane for dye removal from water. J Membr. Sci. 632:119352.

Ma L, Fan H, Li M, Tian H, Fang J, Dong G. (2015) A simple melamine-assisted exfoliation of polymeric graphitic carbon nitrides for highly efficient hydrogen production from water under visible light. J Mater. Chem. A.3(44):22404-12.

Mahmoodi NM, Ghadirli MM, Hayati B, Mahmoodi B, Rabeie B. (2025) Synthesis of ZIF-8 composite (g-C_3N_4@ ZIF-8/Ag_3PO_4) as a catalyst for the malachite green and tetracycline degradation. Inorg. Chem. Commun. 177:114345.

Martínez C, Vilariño S, Fernández M, Faria J, Santaballa J. (2013) Mechanism of degradation of ketoprofen by heterogeneous photocatalysis in aqueous solution. Appl Catal B-Environ.142:633-46.

Mei, Q., Qiu, Z., Jiang, J., Li, M., Wang, Q., & He, M. (2025). Ozonolysis of ketoprofen in polluted water: Reaction pathways, kinetics, removal efficiency, and health effects. J Environ. Sci., 1*47*, 451-461.

Nguyen Van M, Mai OLT, Pham Do C, Lam Thi H, Pham Manh C, Nguyen Manh H, et al. (2020) Fe-doped g-C_3N_4: High-performance photocatalysts in rhodamine B decomposition. Polymers.12(9):1963.

Park KS, Ni Z, Côté AP, Choi JY, Huang R, Uribe-Romo FJ, et al. (2006) Exceptional chemical and thermal stability of zeolitic imidazolate frameworks. Proceedings of the National Academy of Sciences.103(27):10186-91.

Payra S, Challagulla S, Bobde Y, Chakraborty C, Ghosh B, Roy S. (2019) Probing the photo-and electro-catalytic degradation mechanism of methylene blue dye over ZIF-derived ZnO. J Hazard. Mater.373:377-88.

Pereira RC, Anizelli PR, Di Mauro E, Valezi DF, da Costa ACS, Zaia CTB, et al. (2019) The effect of pH and ionic strength on the adsorption of glyphosate onto ferrihydrite. Geochem. T. 20(1):3.

Prasanna SB, Sakthivel R, Shivamurthy SA, Lin Y-C, Liu X, Chen J-C, et al. (2024) Catalytic degradation of tetracycline using marigold flower-like structure erbium molybdate decorated on sulphur-doped g-C_3N_4 nanocomposite: Kinetics, thermodynamics, DFT calculations, and toxicity studies. Sep. Purif. Tech. 330:125439.

Qiu M, Liu Z, Wang S, Hu B. (2021) The photocatalytic reduction of U (VI) into U (IV) by ZIF-8/g-C_3N_4 composites at visible light. Environ. Res. 196:110349.

Rani M, Shanker U, Chaurasia AK. (2017) Catalytic potential of laccase immobilized on transition metal oxides nanomaterials: degradation of alizarin red S dye. J Environ. Chem. Eng. 5(3):2730-9.

Sairaj V, Poovethamkandiyil AS, Anas S, Hinder SJ, Pillai SC, Vijayan BK. (2024) One pot synthesis of multi-functional B doped g-C3N4-praseodymium oxide nanocomposites for colorimetric detection of Hg^{2+} ion and solar photocatalytic removal of toxic water pollutants. J Water Process Eng. 62:105341.

Schelling M, Kim M, Otal E, Aguirre M, Hinestroza JP. (2020) Synthesis of a zinc–imidazole metal–organic framework (ZIF-8) using ZnO rods grown on cotton fabrics as precursors: arsenate absorption studies. Cellulose.27:6399-410.

Shaalan RA, Haggag RS, Belal SF, Agami M. (2013) Simultaneous determination of hyoscine, ketoprofen and ibuprofen in pharmaceutical formulations by HPLC-DAD. J Appl. Pharm. Sci. 3(7):038-47.

Sharma SK, Kumar A, Sharma G, Wang T, Iglesias-Juez A, Dhiman P. (2023) Recent advances in g-C3N4/Metal organic frameworks heterojunctions for high-performance photocatalytic environmental remediation and energy production. J Mol. Liq. 382:121890.

Sun Y, Zhang H, Lv Y, An S, Wang R. ZIF-8/gC_3N_4 photocatalysts: enhancing CO 2 reduction through improved adsorption and photocatalytic performance. RSC advances. 2024;14(25):17498-506.

Suresh R, Karthikeyan N, Gnanasekaran L, Rajendran S, Soto-Moscoso M. (2023) Facile synthesis of CuO/g-C_3N_4 nanolayer composites with superior catalytic reductive degradation behavior. Chemosphere.315:137711.

Verma R, Chauhan MS, Pandey S, Dandia A. (2023) Reduced graphene Oxide/NiO based nano-composites for the efficient removal of alizarin dye, indigo dye and reduction of nitro aromatic compounds. Heliyon.

Wang Y, Zhao S, Zhang Y, Chen W, Yuan S, Zhou Y, et al. (2019) Synthesis of graphitic carbon nitride with large specific surface area via copolymerizing with nucleobases for photocatalytic hydrogen generation. Appl. Surf. Sci. 463:1-8.

Xu T, Guan S-X, Tang L, Zhang J-Y, Luo C, Wang H, et al. (2023) The enhanced charge separation over dual Z-scheme MoS_2@ g-C_3N_4/ZIF-8 (Zn) photocatalyst: the boosted Fenton activation model and DFT calculation. J Photoc. Photobio. A: Chemistry.441:114756.

Xue J, Huang C, Xu P, Wang M, Ma S. (2019) Facile one-step synthesis of broken case-like carbon-doped g-C3N4 for photocatalytic degradation of benzene. Appl. Organomet. Chem. 33(7):e4966.

Yang Q, Lin W, Duan Z, Xu S, Chen J, Mai X. (2023) Bismuth-doped g-C_3N_4/ZIF-8 heterojunction photocatalysts with enhanced photocatalytic performance under visible light illumination. Environ. Tech. 44(8):1156-68.

Yaseen BM, Albadr RJ, Jain V, Kumar A, Ballal S, Singh A, et al. (2025) Synthesis of novel g-C_3N_4/ZIF-8/$MnFe_2O_4$ nanocomposite: efficient heterogeneous photocatalyst for degradation of tetracycline hydrochloride. J Mater. Sci.-Mater El.36(5):299.

Yuan X, Qu S, Huang X, Xue X, Yuan C, Wang S, et al. (2021) Design of core-shelled g-C3N4@ ZIF-8 photocatalyst with enhanced tetracycline adsorption for boosting photocatalytic degradation. Chem.Eng. J 416:129148.

Zhao Z, Ma Y, Fan J, Xue Y, Chang H, Masubuchi Y, et al. (2018) Synthesis of graphitic carbon nitride from different precursors by fractional thermal polymerization method and their visible light induced photocatalytic activities. J Alloy Compd. 735:1297-305.

Zheng W, Feng S, Feng S, Shao C, Jiang Z, Wu W, et al. (2021) The gC 3 N 4 modified by AgBr and ZIF-8 adsorption-photocatalysis synergistic degradation of bisphenol A. Res. Chem. Intermediat. 47:1471-87.

Zheng W, Feng S, Feng S, Shao C, Jiang Z, Wu W, et al. (2021) The g-C_3N_4 modified by AgBr and ZIF-8 adsorption-photocatalysis synergistic degradation of bisphenol A. Res. Chem. Intermediat. 47(4):1471-87.

Zhou J, Liu W, Cai W. (2019) The synergistic effect of Ag/AgCl@ ZIF-8 modified g-C3N4 composite and peroxymonosulfate for the enhanced visible-light photocatalytic degradation of levofloxacin. Sci.Total Environ. 696:133962.

Zhou S, Liu Y, Li J, Wang Y, Jiang G, Zhao Z, et al. (2014) Facile in situ synthesis of graphitic carbon nitride (g-C_3N_4)-N-TiO2 heterojunction as an efficient photocatalyst for the selective photoreduction of CO2 to CO. Appl. Catal. B: Environ.158:20-9.